The Astrophysical Journal, 696:1526–1532, 2009 May 10 doi:10.1088/0004-637X/696/2/1526

FORMATION HEIGHTS OF EXTREME ULTRAVIOLET LINES IN AN ACTIVE REGION DERIVED BY CORRELATION OF DOPPLER VELOCITY AND MAGNETIC FIELD

Y. Guo[1], M. D. Ding[1], M. Jin[1], and T. Wiegelmann[2]
[1] Department of Astronomy, Nanjing University, Nanjing 210093, China; dmd@nju.edu.cn
[2] Max-Planck-Institut für Sonnensystemforschung, Max-Planck-Strasse 2, 37191 Katlenburg-Lindau, Germany; wiegelmann@mps.mpg.de
Received 2008 November 18; accepted 2009 February 25; published 2009 April 24

ABSTRACT

We study the correlation heights, which indicate the formation height of Extreme Ultraviolet (EUV) lines in an active region using observations from the EUV Imaging Spectrometer and Solar Optical Telescope on board *Hinode*. The nonlinear force-free field optimization method is adopted to extrapolate the three-dimensional magnetic fields to higher layers. Three subregions with different characteristics are selected in the active region for this study. The results show that the formation heights in different subregions vary with their different magnetic fields or velocity patterns. After solving the line blending problem between the He II 256.32 Å and Si X 256.37 Å lines by the double Gaussian curve fitting, we find that the transition region lies higher in a strong magnetic area. In a preflare heating area, there possibly exist multithermal loops as implied by comparing the Doppler velocity and the magnetic field on the solar disk.

Key words: Sun: corona – Sun: magnetic fields – Sun: transition region – Sun: UV radiation

1. INTRODUCTION

The correlation height, defined as the height at which the correlation coefficient between the Doppler velocity of extreme ultraviolet (EUV) lines and the magnetic field inclination reaches its maximum, can be used to represent the formation altitude of EUV lines (Tu et al. 2005a, 2005b). There are two reasons for this. On the one hand, the magnetic field controls the plasma motion in the transition region and corona, where the low β condition takes the responsibility. The plasma moves mainly along the magnetic field lines. Therefore, the line-of-sight component of the velocity should be proportional to the cosine of the angle between the magnetic field lines and the line of sight, or the magnetic field inclination. Consequently, the absolute value of the Doppler velocity has a positive correlation with the value of $|B_z/B|$, where B is the magnetic field strength and B_z is the line-of-sight component. Note that the Cartesian coordinate system is adopted here. On the other hand, the EUV line intensity from an optically thin plasma is proportional to the integration $\int_V G(T)n_e^2 dV$, where $G(T)$ is the contribution function for plasma with temperature T, and n_e is the electron density (Watanabe et al. 2007). Although the volume V has a spatial extension, the contribution function $G(T)$ peaks sharply at a temperature $T_{\max}$. The line emission is mostly from the plasma with temperature $T_{\max}$. Therefore, we can take the height where the temperature reaches $T_{\max}$ as the EUV line formation altitude.

The formation heights of EUV lines are very important for us to understand the structure of the solar upper atmosphere, which has been simulated through three-dimensional MHD numerical modeling (Gudiksen & Nordlund 2005) and synthesis of coronal emission lines (Peter et al. 2004). However, it is difficult to deduce the formation height from observations. The first effort has been made by Tu et al. (2005a) who studied the transition region lines in the quiet Sun by the correlation method. Tu et al. (2005b) further proposed the funnel model for solar wind origin. Marsch et al. (2006) studied the structure of the solar transition region in a polar coronal hole, and found that the correlation heights differ in the open magnetic field region and the closed one even for the same emission line. Marsch et al. (2004, 2008) and Wiegelmann et al. (2005) studied the link between plasma flows and magnetic fields in the active regions and in an equatorial coronal hole, respectively. The emission heights of coronal bright points derived from the correlation of Fe XII intensity enhancement and the magnetic fields have been discussed in Tian et al. (2007). With the correlation method, Tian et al. (2008) studied the sizes of transition region structures in coronal holes and the adjacent quiet Sun. Moreover, the magnetic field structure of quiet Sun and coronal holes has been investigated with the help of a potential field model in Wiegelmann & Solanki (2004) and compared with transition region and coronal EUV images.

The correlation method mentioned above needs the combination of observed EUV lines and three-dimensional magnetic fields, the latter of which are usually obtained by force-free field extrapolation of the measured fields in the lower solar atmosphere, such as the photosphere. In previous papers, a linear force-free field (LFFF) model (Wiegelmann & Neukirch 2002) or potential field model was adopted. Recently, a new nonlinear force-free field (NLFFF) optimization method was proposed by Wheatland et al. (2000) and implemented by Wiegelmann (2004), which has been widely used for the extrapolation of three-dimensional magnetic fields. The NLFFF extrapolation method is more accurate for magnetic field reconstruction especially in active regions (Schrijver et al. 2006; Metcalf et al. 2008), where the magnetic fields are highly sheared and twisted, the electric current is large, and the force-free parameter α usually changes through the space. The potential field and the LFFF model are inadequate for these active regions. A review on this topic can be found in Wiegelmann (2008).

In this paper, we study the correlation heights between the Doppler velocity of EUV lines and the magnetic field inclination in an active region with the observations of EUV Imaging Spectrometer (EIS; Culhane et al. 2007) and Solar Optical Telescope (SOT; Tsuneta et al. 2008; Suematsu et al. 2008; Ichimoto et al. 2008; Shimizu et al. 2008) on board *Hinode* (Kosugi et al. 2007). In particular, we adopt the NLFFF optimization method implemented by Wiegelmann

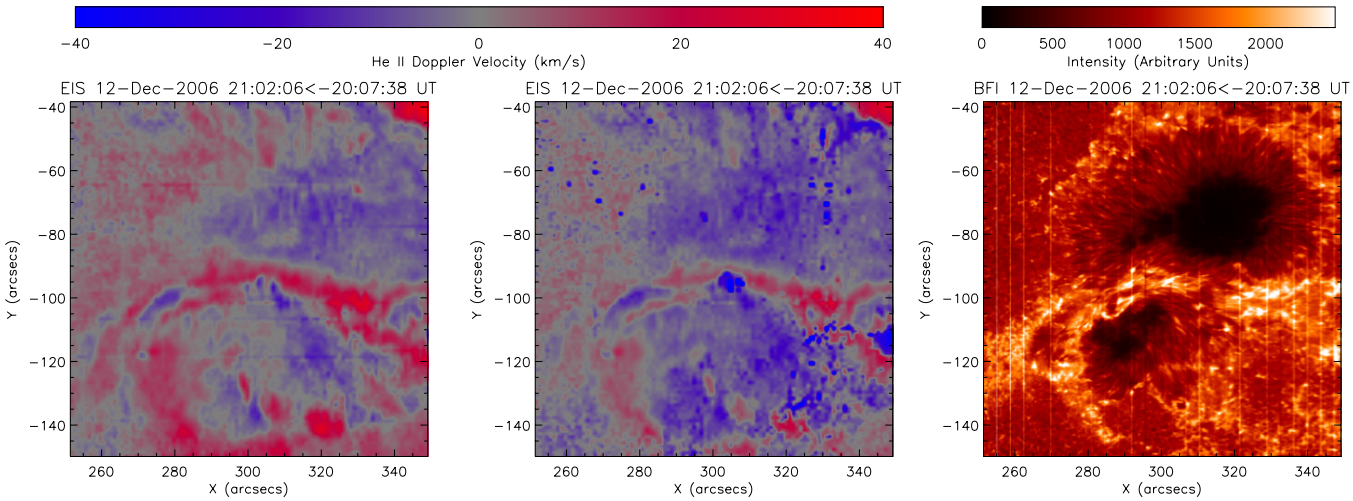

Figure 1. EIS He II 256 Å velocity maps fitted by a single Gaussian curve (left panel) and double Gaussian curves (middle panel). The velocities that exceed 40/−40 km s^{-1} have been set to the top color (red/blue) in order to make the velocity field pattern stand out. The Ca II H image (right panel) shows that it has similar configurations with the He II 256 Å velocity maps. The Ca II H image observed by SOT/BFI is created artificially to match the EIS map in time. See text for details.

(2004) to extrapolate the three-dimensional magnetic fields. Three subregions with different characteristics are selected in the active region for this study. The details of data analysis and image co-alignment are described in Section 2. Results are presented in Section 3. Discussion and conclusions are made in Section 4.

2. OBSERVATIONS AND DATA ANALYSIS

2.1. EIS Doppler Velocity Fitting

We select six EUV emission lines as shown in Table 1 to calculate the correlation heights. The six emission lines cover a relatively large range of formation temperatures from the transition region to the corona. They were obtained by the EIS 1″ × 256″ slit scanning from west to east during 19:07–23:46 UT on 2006 December 12 in the active region NOAA 10930. The exposure time is 30 s for each slit. We apply the standard EIS procedure to calibrate the data and fit the lines with single Gaussian curve. The Doppler velocities can be calculated by the line center shifts. When determining the center of a specific line, two instrumental effects should be taken into account. One is the slit tilt, because the EIS slit is not perfectly parallel to the pixel array of the CCD. The other is the orbital variation, which is caused by thermal effect on the instrument and follows a sinusoidal behavior. To remove the former, we subtract the Doppler shift taken early in the mission (regarded as purely due to the tilt effect) from the current one. To remove the latter, we first set a rest line center position for each raster which is taken to be the average of the southern part (a relatively quiet region) of each slit. Then the time variation of the rest line center relative to its theoretical position in laboratory is obtained. After the above steps, we can finally construct the Dopplergrams for each line.

The average values of χ^2 in the line profile fitting in some regions of interest, which will be defined in Section 2.4, are shown in Table 1. They are relatively small for Fe VIII, Fe X, Fe XIII, and Fe XV lines compared to He II and Fe XI lines in all the regions, since the latter two lines are blended with other lines. The He II 256.32 Å line is blended with the Si X 256.37 Å line, especially in active regions and magnetic loops. Therefore, we use double Gaussian curves to fit the two components with only one assumption that the blueward component corresponds to the He II line. The Fe XI line is a doublet at 188.23 Å and 188.30 Å (Young et al. 2007a). We also fit it by double Gaussian curves assuming that the 188.23 Å component lies blueward. Note that the double Gaussian curve fitting is sensitive to the selection of initial values, in particular the line center wavelengths. Here, we set them to be the rest wavelengths of each line. The fitting yields seven parameters, including the amplitudes, widths, and central wavelengths for both components, and a shared background. The result of double Gaussian curve fitting for the He II line is shown in Figure 1 and Table 1. We find that the average velocities are more blueshifted compared to the result from single Gaussian curve fitting, as expected. In particular, the χ^2 values are much smaller in the former case as show in Table 1, implying that the fitting goodness is significantly improved. The result for the Fe XI 188.23 Å line is similar to the He II line.

The non-Gaussian line profiles of EIS in this active region have been reported by Imada et al. (2008), who fitted the Fe XIV 274.20 Å line in the arcades during the flare. Asai et al. (2008) performed the first spectroscopic observation of an MHD fast mode shock wave during the flare using double Gaussian curve fitting of the lines. Here, we analyze the lines before the flare.

2.2. Magnetic Field Extrapolation

The active region NOAA 10930 has been studied by many authors (Kubo et al. 2007; Zhang et al. 2007; Jing et al. 2008; Schrijver et al. 2008; Wang et al. 2008). Guo et al. (2008) extrapolated the three-dimensional magnetic field using the NLFFF optimization method and studied the configuration, energy release, and shear angle changes in this active region. The photospheric vector magnetic fields are obtained by fitting the polarized spectrum observed by SOT/SP (spectropolarimeter), which scanned the southwestern part of the solar disk from 20:30 to 21:33 UT on 2006 December 12. In the fast map mode, the spatial sampling of SOT/SP is about 0.″3. The spectra are fitted by a nonlinear least-square fitting procedure based on the Milne–Eddington model. The 180° ambiguity of the azimuth angle is removed by comparing the observed field to the extrapolated LFFF field (Wang 1997; Wang et al. 2001; Metcalf et al. 2006). The top left panel in Figure 2 shows the full field of view (FOV) of the magnetic field observed by SOT/SP. We select half of the FOV and sample them to 128 × 128 grids

Table 1
EIS Emission Lines, Average Doppler Velocities, and Average Values of χ^2 for the Line Profile Fitting in Three Selected Regions

Ion	Wavelength (Å)	log T_{max}	Average Doppler Velocity[a] (km s^{-1})			Average χ^2 [a]		
He II[b].....	256.32	4.9	−9.8	4.3	−0.3	1.6	5.0	3.3
He II[c].....			−12.9	1.7	−2.7	0.5	0.4	0.5
Fe VIII.....	185.21	5.6	−21.9	1.6	−5.2	0.3	0.3	0.3
Fe X.....	184.54	6.0	−27.5	1.2	−13.8	0.4	0.7	0.6
Fe XI[b].....	188.23	6.1	−15.4	−1.0	−9.9	2.5	12.4	10.1
Fe XI[c].....			−25.3	−9.7	−14.4	0.5	0.3	0.5
Fe XIII.....	202.04	6.2	−24.3	−4.0	−10.9	0.3	0.4	0.4
Fe XV.....	284.16	6.3	−11.8	−5.3	−1.7	0.7	2.0	1.2

Notes.
[a] The values in the three columns are calculated for Regions 1–3, which are defined in Figure 4.
[b] The average velocities and χ^2 for this line are calculated by single Gaussian curve fitting.
[c] The average velocities and χ^2 for this line are calculated by double Gaussian curve fitting.

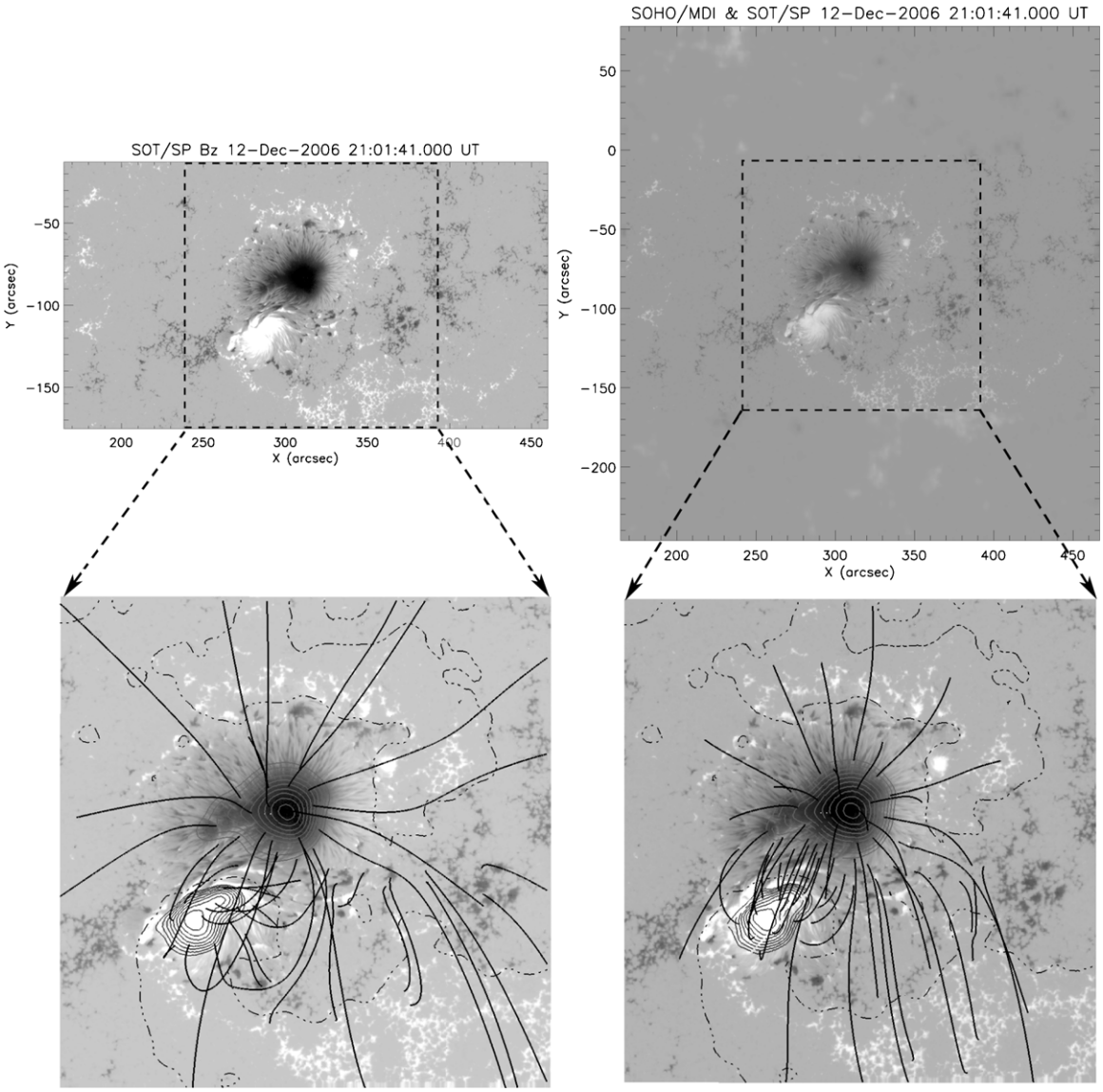

Figure 2. Top left: the FOV of the magnetic field observed by SOT/SP from 20:30 to 21:33 UT on 2006 December 12. The dashed square denotes the FOV in which the NLFFF extrapolation is performed. Bottom left: the three-dimensional magnetic field extrapolated by the NLFFF model for the dashed square shown in the top left panel. Top right: the FOV of MDI magnetogram for potential field extrapolation observed at 20:51 UT on 2006 December 12. The dashed square is the similar to that in the top left panel. Bottom right: the three-dimensional magnetic field extrapolated by the potential field model. Note that only the region in the dashed square is shown.

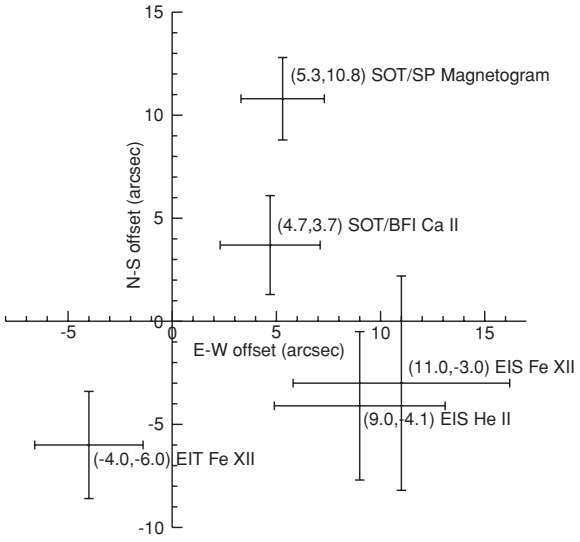

Figure 3. Offsets of images observed by different instruments with respect to MDI. Positive values in the parentheses show that image shifts to east or south, while negative values to west or north. The error bars are also plotted, both in the east–west and the north–south directions.

by 4 × 4 binning due to the limitation in computations. Then the boundary data are preprocessed by a preprocessing routine developed by Wiegelmann et al. (2006). The final extrapolation result by the NLFFF optimization method (Wheatland et al. 2000; Wiegelmann 2004) is shown in the bottom left panel of Figure 2.

We adopt the potential field model to extrapolate the magnetic field in a larger FOV, because the extrapolation height of SOT/SP magnetic field is limited to ∼110 Mm and the potential field model needs only the line-of-sight component of the field, which can be obtained in the MDI full disk observations. The FOV of MDI data used for extrapolation is shown in Figure 2 (top right), but the data in the area corresponding to the FOV of the top left panel are replaced by SOT/SP magnetic fields. This is because that the MDI data suffer from the saturation problem, which is discussed in detail in a previous paper (Moon et al. 2007). We extrapolate the fields with the Fourier transform method (Alissandrakis 1981; Gary 1989) in this larger FOV that is four times the FOV used in the NLFFF method. The boundary data are sampled to 256 × 256 grids with spatial resolution of ∼1.″2. So the extrapolation height is ∼220 Mm. The three-dimensional magnetic field is shown in Figure 2 (bottom right). In order to calculate the correlation heights, we have to align the EUV images with the SOT/SP images. This is done by correlating the two set of images and finding the offsets between them.

2.3. *Co-alignment of* Hinode *Observations*

EIS covers two wavelength bands, i.e., short wavelength (SW) band (170–211 Å) and long wavelength (LW) band (246–292 Å), which are recorded by two CCDs, respectively. Images on the SW CCD have an offset of 16″–20″ northward and 2″ westward compared to that on the LW CCD (Young et al. 2007b). We correct for the offsets in SW images by applying a fixed value of 16″ in the north–south direction and 2″ in the east–west direction. We also need to align the SW and the LW images with the magnetograms. The main idea is to align all the images by EIS and SOT with that by EUV Imaging Telescope (EIT; Delaboudinière et al. 1995) and Michelson Doppler Imager (MDI; Scherrer et al. 1995) on the *Solar and Heliospheric Observatory* (*SOHO*). The full disk images by EIT and MDI enable us to align them by comparing the limbs. The accuracy is close to their spatial resolutions. Since the EIS and SOT observations are within a partial disk, we cannot get the absolute coordinates of the solar disk center. However, after being aligned with the MDI images, all the coordinates are referred to the true solar disk center.

The SOT/SP magnetogram is aligned with the MDI magnetogram as follows. First of all, the two images are interpolated to the same resolution, always to the better one. Then, we select two slit images to do the correlation, because the MDI magnetogram was observed during the scanning time of the SOT/SP one, i.e., 20:30–21:33 UT. The slit image of SOT/SP that has the closest time to the MDI observation is correlated with the MDI slit images in different positions. Finally, the offset is found for which the two slit images have the largest correlation coefficient. The uncertainty of the co-alignment is about 2.″0.

The EIS Fe XII 195 Å image is aligned with the EIT Fe XII 195 Å image with the correlation method too. Then the EIT 195 Å image is aligned with the MDI magnetogram by comparing the limbs. Reading the coordinates of the east, west, south, and north poles on the solar limb in the MDI magnetogram, we calculate the coordinates of the disk center and find that the coordinates provided by MDI are correct. But the EIT 195 Å image taken at 23:49 UT on the same day, which is the closest to the EIS observation, shifts 4.″0 westward and 6.″0 northward in the coordinates provided by the standard software. The uncertainty of the shift is ∼2.″6, which is the resolution of EIT images. Finally, The offset between the EIS Fe XII 195 Å image and the MDI image is found. The total uncertainty is ∼5.″2.

The EIS He II 256 Å velocity map is aligned with the SOT/BFI (Broadband Filter Imager) Ca II H image, the SOT/SP and MDI magnetograms consecutively. We find that the redshift region of the He II velocity map has similar configurations with the heating region of the Ca II H image as shown in Figure 1. Note that the Ca II H image was observed every 2 minutes, but the EIS map was constructed from raster scanning during about 4.5 hr. We need to reconstruct a Ca II H image in the exactly same manner as the EIS map. To do so, we cut the Ca II H images at each time into slices along the slit. We pick out the slice with the same position and time as each slit in EIS scanning observations. Then we adopt a feature identification method to align them, i.e., select points with similar features alternately from the two images. Usually we select five points from each image to calculate an offset and repeat it 10 times to estimate the uncertainties. The average offsets in the *x*- and *y*-directions are 4.″3 and −7.″8, with errors of 1.″7 and 1.″2, respectively. Next, the Ca II H image is aligned with the SOT/SP magnetogram with the identification method, too. The offset in the *x*-direction is −0.″6 with an error of 0.″4, and that in the *y*-direction is −7.″1 with an error of 0.″4. Because the SOP/SP magnetogram has already been aligned with the MDI magnetogram, the EIS He II velocity map can be aligned with the latter with total uncertainties of 4.″1 and 3.″6 along the *x*- and *y*-directions, respectively.

We plot the offsets of all images with respect to the MDI image in Figure 3. If we adopt the offsets between SW and LW images given by Young et al. (2007b), we only have to align one of them with MDI magnetograms. Then the other can be aligned automatically. But here we align both with independent methods to check the offsets derived by us and by them. The LW and SW images have the same offsets with respect to

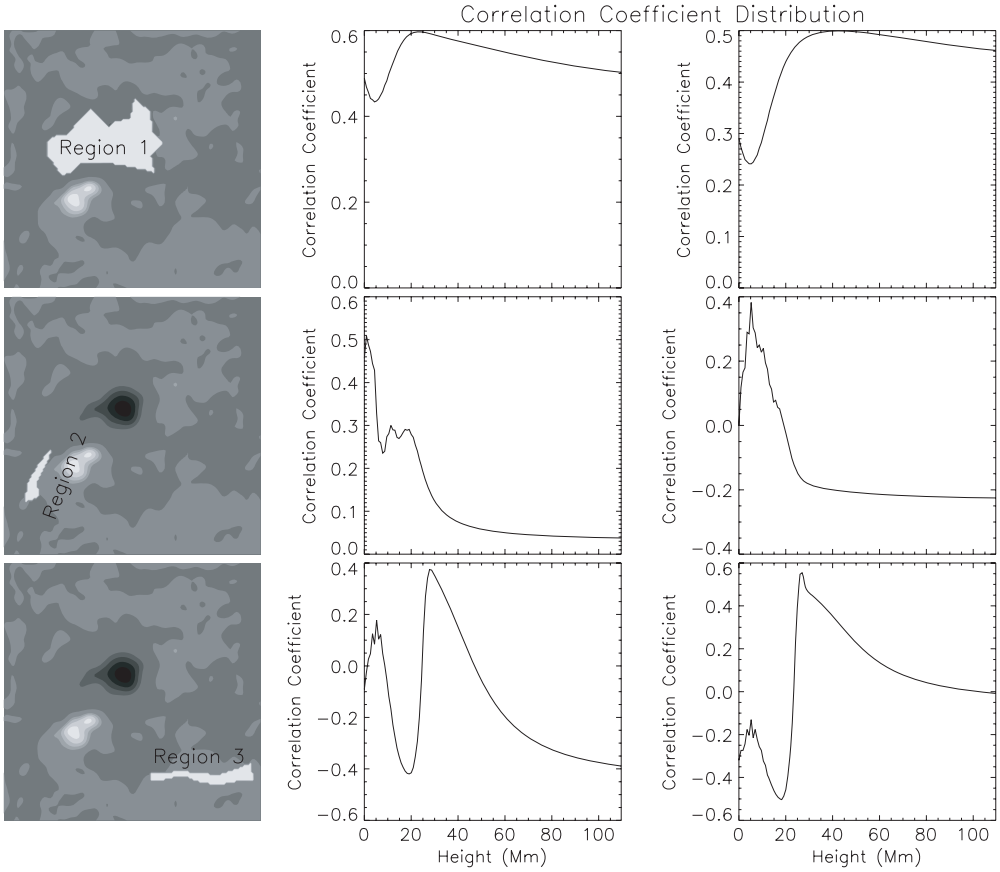

Figure 4. Height distributions of the correlation coefficient for the He II 256 Å line in different subregions of the active region NOAA 10930. The white polygons labeled with Regions 1–3 (left column) show the areas selected to calculate the correlation coefficients. The distributions in the middle and right columns are calculated by correlating the magnetic field inclination with the Doppler velocity, which is obtained by single and double Gaussian curve fitting, respectively. The distributions in top to bottom rows are obtained in Regions 1–3, respectively.

MDI magnetogram within the uncertainties, which indicates our results are coincident with theirs.

2.4. Correlation Heights and Error Estimation

We select different regions to calculate the correlation coefficients that are plotted in Figure 4. Different from quiet Sun regions, the environment in active region is quite inhomogeneous. It is necessary to select different subregions to calculate the correlation heights. The high spatial resolution observations of *Hinode* provide us the possibility of doing so. The subregions are selected according to spatial patterns of the magnetic fields and velocity fields; so their shapes are not necessarily regular. Region 1 mainly concentrates on the negative magnetic polarity region and the blueshift area of He II 256 Å. Region 2 is on the east side of the polarity inversion line, corresponding to the foot points of some lower loops and the redshift area of He II 256 Å. Region 3 is within the projection area of the higher closed magnetic loops. The correlation coefficient distributions are calculated by correlating the magnetic field inclination with the Doppler velocity, which is obtained by single (middle column) and double (right column) Gaussian curve fitting in Figure 4, respectively. The height is less than 5 Mm in Region 2, but more than 20 Mm in Regions 1 and 3. For different lines listed in Table 1, the correlation heights can be calculated with the same method.

There are errors in the image co-alignment, which also cause errors in calculations of the correlation height. As mentioned in Section 2.3, there is an offset between SW and LW EIS images. Moreover, different lines in the same band have internal pointing shifts, which are 0.″5 in the *x*-direction and 1″ in the *y*-direction for SW and 3″ in the *x*-direction and 4″ in the *y*-direction for LW as shown in a preliminary research by Deb[3]. Taking into account these facts, the errors in the image co-alignment are 7.″7 in the *x*-direction and 8.″2 in the *y*-direction for SW except for Fe XII 195 Å. They are 7.″1 in *x*-direction and 7.″6 in the *y*-direction for LW except for He II 256 Å. The errors of the correlation height are estimated by the following way. First, we artificially shift the EIS velocity map relative to the magnetic field B_z image within the range of co-alignment errors. Then, the correlation heights are calculated for each case (here, we select $1'' \times 1''$ grids). Finally, we get a grid of correlation heights with different correlation coefficients. The final correlation height for one specific line is estimated as the average of the heights with correlation coefficients greater than 0.07, and the error is the standard deviation of these heights.

3. RESULTS

The average formation height of He II 256 Å in Region 2 is lower than that in Regions 1 and 3. In comparison, the mean magnetic fields in Regions 2 and 3 are 1 order of magnitude weaker than that in Region 1. This implies that stronger magnetic fields correspond to higher formation heights of EUV lines. For Regions 2 and 3, the mean magnetic fields are almost the same, but the Doppler velocity patterns are different, which

[3] http://msslxr.mssl.ucl.ac.uk:8080/eiswiki/Wiki.jsp?page=FitsPointing

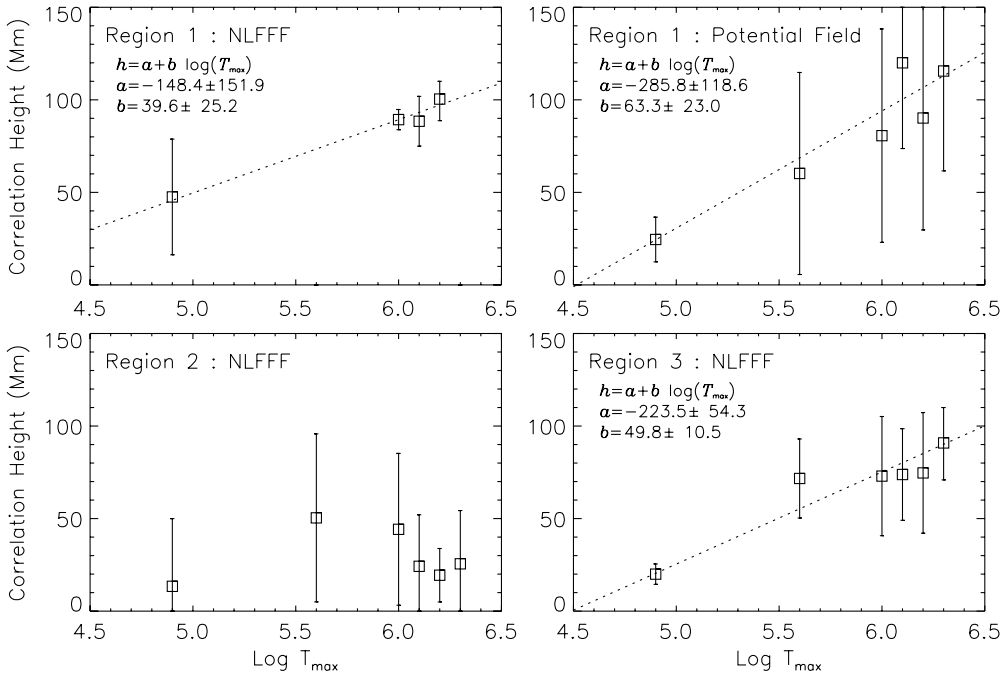

Figure 5. Correlation heights vs. log T_{max} for Regions 1–3. The magnetic field is extrapolated with the NLFFF model except for the top right panel, in which the potential field model is used. The dotted lines are the linear fitting of the height–log T_{max} relationship.

show mainly redshifts and blueshifts, respectively. This means that down flows tend to make the formation height lower. In summary, the correlation heights are different in various regions even for the same line He II 256 Å because of different physical conditions.

The correlation height versus log T_{max} is plotted in Figure 5, where the EUV line formation temperature, T_{max}, is listed in Table 1, and the errors of formation heights are derived using the method mentioned in Section 2.4. In Region 1, shown in Figure 5 (top left), there are no points for Fe VIII and Fe XV, since we cannot find the heights with correlation coefficients greater than 0.07. A possible reason is that the real formation height of Fe XV exceeds the NLFFF extrapolation domain, which is about 110 Mm in height. For Fe VIII, we still do not know the reason. The correlation heights for all the EUV lines can be obtained in Region 1 by the potential field extrapolation in Figure 5 (top right), which can reach about 220 Mm in height. For the regions studied here, the heights for the same line calculated with different extrapolation methods differ slightly within the errors. Also, the heights calculated by the potential field give a similar height versus log T_{max} relationship compared to that calculated by the NLFFF. However, the NLFFF gives less uncertainties for the correlation heights and makes the results more confirmative.

Region 2, shown in Figure 5 (bottom left), is a preflare heating area. Massive downflows can be seen in the EIS velocity map (Figure 1). All the EUV lines are formed within a smaller range of heights. The temperature structure is complicated in this area. There is no clear height versus log T_{max} relationship in Region 2, while there are positive relationships in Regions 1 and 3 (bottom right) as shown in Figure 5. But the temperature in Region 3 rises more quickly. For example, log $T_{max} = 6.3$ corresponds to a height of ∼90 Mm in Region 3, compared to $\gtrsim$ 100 Mm in Region 1. This is probably due to the higher magnetic field strength in Region 1, which seems to suppress the temperature increase with height. Therefore, the EUV line formation height is affected by not only the magnetic topology but also the field strength.

We also plot the linear fitting of the height–log T_{max} relationship for Regions 1 and 3 in Figure 5. These curves provide a quantitative description of how the temperature varies with height in the corona.

4. DISCUSSION AND CONCLUSIONS

The EUV lines in an active region are formed at different heights according to the physical conditions of the magnetized atmosphere in situ, including the velocity, density, temperature, and magnetic field. In this paper, we examine some of these factors with the correlation height method by aligning images observed by SOT and EIS. In particular, we find that the transition region, where He II 256 Å is formed, lies higher in areas with strong magnetic fields.

Results from Region 2 show that the EUV emission lines are formed within a relatively narrow height range in the preflare heating loops. A possible scenario is that this region contains coronal loops that are multithermal. Kjeldseth-Moe & Brekke (1998) have shown that some active region loops contain mixtures of plasma of different temperatures. Multithermal plasma has also been found in the transequatorial loops (Brosius 2006). All these researches are based on the analysis of the co-spatial emission lines on the solar limb. While we find a similar result by analyzing the lines on the solar disk and correlating the Doppler velocity and magnetic field.

We thank the referee for constructive comments that helped to improve the paper. *Hinode* is a Japanese mission developed and launched by ISAS/JAXA, with NAOJ as domestic partner and NASA and STFC (UK) as international partners. It is operated by these agencies in cooperation with ESA and NSC (Norway). Y.G., M.D.D., and M.J. were supported by National Natural Science Foundation of China (NSFC) under grants 10878002, 10333040, and 10673004 and by NKBRSF under grant 2006CB806302. T.W. was supported by DLR-grant 50 OC 0501.

REFERENCES

Alissandrakis, C. E. 1981, A&A, 100, 197
Asai, A., Hara, H., Watanabe, T., Imada, S., Sakao, T., Narukage, N., Culhane, J. L., & Doschek, G. A. 2008, ApJ, 685, 622
Brosius, J. W. 2006, ApJ, 636, L57
Culhane, J. L., et al. 2007, Sol. Phys., 243, 19
Delaboudinière, J.-P., et al. 1995, Sol. Phys., 162, 291
Gary, G. A. 1989, ApJS, 69, 323
Gudiksen, B. V., & Nordlund, Å. 2005, ApJ, 618, 1020
Guo, Y., Ding, M. D., Wiegelmann, T., & Li, H. 2008, ApJ, 679, 1629
Ichimoto, K., et al. 2008, Sol. Phys., 249, 233
Imada, S., Hara, H., Watanabe, T., Asai, A., Minoshima, T., Harra, L. K., & Mariska, J. T. 2008, ApJ, 679, L155
Jing, J., Wiegelmann, T., Suematsu, Y., Kubo, M., & Wang, H. 2008, ApJ, 676, 81
Kjeldseth-Moe, O., & Brekke, P. 1998, Sol. Phys., 183, 73
Kosugi, T., et al. 2007, Sol. Phys., 243, 3
Kubo, M., Yokoyama, T., & Katsukawa, Y., et al. 2007, PASJ, 59, S779
Marsch, E., Tian, H., Sun, J., Curdt, W., & Wiegelmann, T. 2008, ApJ, 685, 1262
Marsch, E., Wiegelmann, T., & Xia, L. D. 2004, A&A, 428, 629
Marsch, E., Zhou, G.-Q., He, J.-S., & Tu, C.-Y. 2006, in Proc. Eur. Space Agency, 617, ed. H. Lacoste & L. Ouwehand (Noordwijk: ESA Publications), 100
Metcalf, T. R., et al. 2006, Sol. Phys., 237, 267
Metcalf, T. R., et al. 2008, Sol. Phys., 247, 269
Moon, Y.-J., et al. 2007, PASJ, 59, S625
Peter, H., Gudiksen, B. V., & Nordlund, Å. 2004, ApJ, 617, L85
Scherrer, P. H., et al. 1995, Sol. Phys., 162, 129
Schrijver, C. J., et al. 2006, Sol. Phys., 235, 161
Schrijver, C. J., et al. 2008, ApJ, 675, 1637
Shimizu, T., et al. 2008, Sol. Phys., 249, 221
Suematsu, Y., et al. 2008, Sol. Phys., 249, 197
Tian, H., Marsch, E., Tu, C.-Y., Xia, L.-D., & He, J.-S. 2008, A&A, 482, 267
Tian, H., Tu, C.-Y., He, J.-S., & Marsch, E. 2007, Adv. Space Res., 39, 1853
Tsuneta, S., et al. 2008, Sol. Phys., 249, 167
Tu, C.-Y., Zhou, C., Marsch, E., Wilhelm, K., Zhao, L., Xia, L.-D., & Wang, J.-X. 2005a, ApJ, 624, L133
Tu, C.-Y., Zhou, C., Marsch, E., Xia, L.-D., Zhao, L., Wang, J.-X., & Wilhelm, K. 2005b, Science, 308, 519
Wang, H. 1997, Sol. Phys., 174, 265
Wang, H., Jing, J., Tan, C., Wiegelmann, T., & Kubo, M. 2008, ApJ, 687, 658
Wang, H., Yang, Y., & Sakurai, T. 2001, Sol. Phys., 201, 323
Watanabe, T., Hara, H., Culhane, L., Harra, L. K., Doschek, G. A., Mariska, J. T., & Young, P. R. 2007, PASJ, 59, S669
Wheatland, M. S., Sturrock, P. A., & Roumeliotis, G. 2000, ApJ, 540, 1150
Wiegelmann, T. 2004, Sol. Phys., 219, 87
Wiegelmann, T. 2008, J. Geophys. Res., 113, A03S02
Wiegelmann, T., Inhester, B., & Sakurai, T. 2006, Sol. Phys., 233, 215
Wiegelmann, T., & Neukirch, T. 2002, Sol. Phys., 208, 233
Wiegelmann, T., & Solanki, S. K. 2004, Sol. Phys., 225, 227
Wiegelmann, T., Xia, L. D., & Marsch, E. 2005, A&A, 432, L1
Young, P. R., et al. 2007a, PASJ, 59, S857
Young, P. R., Del Zanna, G., Mason, H. E., Doschek, G. A., Culhane, L., & Hara, H. 2007b, PASJ, 59, S727
Zhang, J., Li, L. P., & Song, Q. 2007, ApJ, 662, L35